SUPER STAR CLUSTERS IN SBS0335-052E

Rodger I. Thompson[1], Marc Sauvage[2], Robert C. Kennicutt[3], Charles Engelbracht[1], Leonardo Vanzi[4],
and Glenn Schneider[1]

[1] Steward Observatory, University of Arizona, Tucson, AZ 85721, USA; rthompson@as.arizona.edu, cengelbracht@as.arizona.edu, gschneider@as.arizona.edu
[2] Service d' Astrophyscique, CEA/DAPNIA, Centre d' Etudes de Saclay, F- 91191 Gif-sur-Yvette Cedex, France; msauvage@cea.fr
[3] Institute of Astronomy, Cambridge University, Madingley Road, Cambridge CB3 0HA, UK; robk@ast.cam.ac.uk
[4] Pontificia Universidad Catolica de Chile, Department of Electrical Engineering, Av. Vicu na Mackenna 4860, Santiago, Chile; lvanzi@ing.puc.cl

ABSTRACT

As one of the lowest metallicity star-forming galaxies, with a nucleus of several super star clusters (SSCs), SBS0335-052E is the subject of substantial current study. We present new insights on this galaxy based on new and archival high spatial resolution NICMOS and attitude control system images. We provide new measurements and limits on the size of several of the SSCs. The images have sufficient resolution to divide the star formation into compact regions and newly discovered extended regions, indicating a bimodal form of star formation. The star formation regions are dated via the equivalent width of the Paα emission and we find that two of the extended regions of star formation are less than 10 million years old. Our previous finding that stellar winds confine the photo-ionizing flux to small regions around individual stars is consistent with the new observations. This may allow planet formation in what would traditionally be considered a harsh environment and has implications for the number of planets around globular cluster stars. In addition, the images pinpoint the regions of H_2 emission as located in, but not at the center of, the two star-forming super star clusters, S1 and S2.

Key words: galaxies: dwarf – galaxies: individual (SBS0335-052E) – galaxies: starburst – galaxies: star clusters

Online-only material: color figures

1. INTRODUCTION

SBS0335-052 is a blue compact dwarf galaxy at a redshift of 0.0136 (Izotov et al. 1997), a distance of 54.3 Mpc and with an apparent V magnitude of 16.65 (Thuan et al. 1996). The close group of super star clusters (SSCs) in the galaxy's center has been and currently is the subject of intense scrutiny. Thompson et al. (2006, hereinafter TSKEV), provides a recent summary of previous observations and investigations of the SSCs in SBS0335-052E. Part of the attention is due to the extremely low metallicity of the galaxy. The metallicity, as measured by 12 + log(O/H) in SBS0335-052E ranges between 7.20 and 7.31 (Papaderos et al. 2006). SBS0335-052E has the fourth lowest metallicity of any star-forming galaxy, surpassed only by its western companion SBS0335-052W with the lowest measured metallicity, J0956+2849, and the well known I Zw 18 (Izotov & Thuan 2007). Because of its low metallicity and now its intense star formation, possibly due to an encounter with the nearby giant spiral galaxy NGC 1376, it represents star formation and feedback in an environment very much like star formation in the early universe. SBS0335-052E is obviously in a very early stage of its star formation since the observed stellar mass of 8×10^7 $M_{\odot}$ is only about 1/25 of the gas mass of 2.1×10^9 $M_{\odot}$ which is again small relative to the dynamical mass of $9 \times 10^9 M_{\odot}$ (Pustilnik et al. 2001), most of which must be dark matter. A main conclusion of TSKEV was that the majority of photo-ionizing radiation from the stars in the actively star-forming SSCs is absorbed within a few stellar radii, thus delaying the onset of negative feedback due to photoionization. This conclusion is validated in the present study under the assumption that the diffuse Paα flux around the SSCs S1 and S2 is due to in situ stars and not from ionizing flux leaking out of the SSCs.

The TSKEV study relied heavily on *Hubble Space Telescope* Near Infrared Camera and Multi-Object Spectrometer (*HST* NICMOS) camera 3 observations of SBS0335-052E which were part of the SINGS (Kennicutt et al. 2003) large survey of nearby galaxies. The 0.″2 pixel scale of camera 3 is not sufficient to resolve much of the detail of the feedback mechanism on star formation operating in the clusters. To get a higher spatial resolution near infrared picture of the SSCs, new observations with the 0.″075 pixel scale NICMOS camera 2 were taken in the Paα and H_2 filters. The primary goal of this paper is to study in detail the feedback effect of the photoionizing flux generated in the SSCs on past and current star formation. This study also utilizes archival NICMOS camera 2 images in Paα and the broadband filters F160W and F205W from observations taken by K. Johnson (see Section 2). Figure 1 shows the location of all the sources discussed in this paper. Sources S1–S6 are originally designated from WFPC2 images in Thuan et al. (1997). The names of sources S3-Paα, S7, and S8 are ascribed by this work. S3-Paα is considered a separate source from S3 as it is offset from the continuum source S3 and is most likely a completely separate source. S7 is the source that was designated by a question mark (?) in TSKEV and S8 is a diffuse source about 2.″5 west of S1 and S2. Unfortunately, this source is marked as S7 in Papaderos et al. (2006) who did not have the spatial resolution to resolve the source we designate as S7 as a separate source. Unlike the NICMOS camera 3 images used in TSKEV the new, much higher resolution, NICMOS camera 2 images clearly resolve S1 and S2 and detect the separation between S3 and S3-Paα. Sources S3-Paα and S7 only appear as slight extensions of the continuum emission in Figure 1, but are clearly shown in the Paα contours in Figure 2. The Advanced Camera for Surveys (ACS) image in Figure 2 is an archival ACS solar blind channel (SBC) image in the UV F140LP filter (Kunth et al. 2003) which is also discussed in TSKEV.
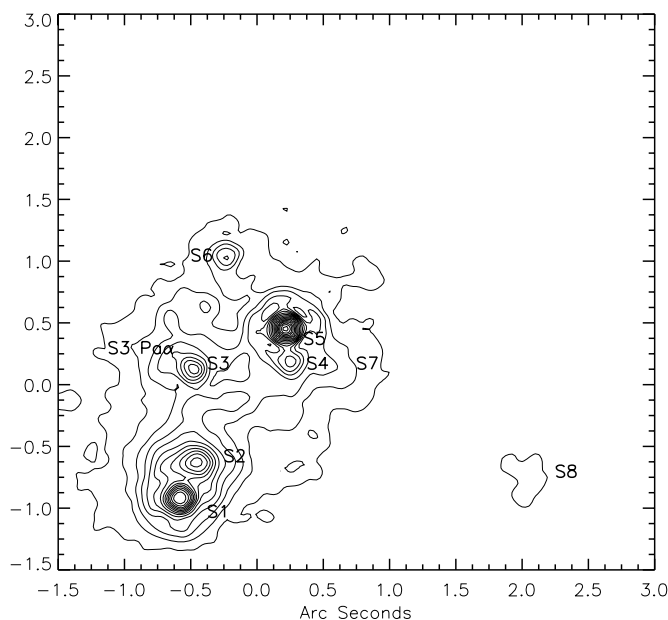
Figure 1. Contour plot of the F160W (1.6 μm) emission from SBS0335-052E. It shows the location of all the sources described in this paper. The sources are displayed with a square root stretch to accommodate the dynamic range of the source strengths. The designations of sources S1–S6 are the sources first named by Thuan et al. (1997). The sources S3-Paα, S7, and S8 are named in this paper. S7 was originally marked as (?) in TSKEV. North is up and east is to the left.

2. OBSERVATIONS

The new observations presented in this paper were taken with the *HST* NICMOS camera 2 in four narrow band filters (F187N, F190N, F212N, and F215N) centered at 1.87 μm, 1.90 μm, 2.12 μm, and 2.15 μm (Proposal ID 10856). These filters are designed to measure Paα and the H$_2$ S(1) lines in the F187N and F212N filters, respectively. The redshift of SBS0335-052, however, shifts these lines to the F190N and F215N filters with the shorter wavelength filters acting as the continuum filters. The program was executed in eight orbits. Exposures were taken in all four filters in each orbit without moving the *HST* during an orbit. During each earth occultation the telescope was dithered one step in a spiral dither pattern with a dither step of 0.''5. The F190N filter which images the strong Paα emission had an integration time of 320 s (Step 32, NSamp=17) and the remaining filters all had integration times of 768 s (Step64, NSamp=20) in each orbit for a total of 2560 s for the F190N filter and 6144 s in each of the remaining filters. The field of view of the NICMOS camera 2 is 19.''5 × 19.''3 which easily encompasses all of the known SSCs.

Additional archival images in the F160W, F205W, F187N, and F190N filters (K. Johnson, Proposal ID 10894; Reines et al. 2008) were also retrieved. There are eight images in the F160W and F205W filters. The F160W images use STEP16 with 26 samples and the F205W images use STEP16 with 24 samples for integration times of 304 and 272 s, respectively. There are 16 on-target images in the F187N and F190N filters, again with STEP16 and 26 samples for F187N and 25 samples for F190N for integration times of 304 and 288 s. The total integration times of the archival images are: F160W, 2432 s; F205W, 2176 s; F187N, 4864 s; F190N, 4600 s.

Archival ACS HRC and WFC1 images of SBS0335-052 from Proposal 10575 (PI Goran Östlin) in F220W, F330W, F550M, F435M filters and the FR656 ramp filter were also retrieved from the STScI MAST archive. The combined drizzled images

are used with no further processing. These images along with previous F122M and F140LP images from Proposal 9470 (PI Daniel Kunth) have been used by Östlin et al. (2008) to make Hα and Lyα images. Table 1 gives a summary of the observational parameters of the images used in this analysis.

Parallel to the NICMOS observations, images of the spiral galaxy NGC 1376 in eight medium band filters were taken with the ACS WFC. Two images in one of the eight filters were taken in each orbit. The ACS observations will be described in a separate publication. SBS0335-052 is probably engaged in a minor merger with NGC 1376 and the images were taken to see if there is any evidence of the interaction. No obvious signs of tidal disruption were seen in the NGC 1376 images. Given the small mass of SBS0335-052 relative to NGC 1376, the absence of any disruption is not surprising.

3. DATA REDUCTION

All the images were reduced with the NICMOS IDL based pipeline procedures operating on the raw frames as described in Thompson et al. (2005). The new images and the archival images were aligned separately since they were at different orientations and had separate dither patterns. The new images were aligned using offsets determined from the F190N image. The position of the pointlike object S1, described below, was determined by centroiding with the IDL procedure IDP3 (Lytle et al. 1999) for each image. The same offsets were used for the other images in each orbit since *HST* was not moved during an orbit. The images in each filter were offset in IDP3 to the position of the images in the first orbit and then median combined. During processing visual inspection showed that two images, one line image and one continuum image, were affected by a cosmic ray persistence streak. This occurs when there is a strong cosmic ray event before the integration begins and the image of the event persists in subsequent images. The pixels involved in the event were identified and were not used in the formation of the median image. This means that the median is formed from only seven images rather than eight for those pixels. The archival images were aligned separately, using the image of S1 in each filter as the fidelity of the pointing between images was not accurately known.

Subtraction of the associated narrow filter continuum image from the image in the emission line filter produces an emission line image. The continuum images are scaled by the known responses of the line and continuum filters and detector QE and subtracted from the line image to produce a continuum-free image. The spacing between the narrow line and continuum filters is only 0.03 μm; therefore the spectral slope of the SEDs, determined from the ground-based spectra of Vanzi et al. (2000), has a negligible effect on the calculated line power. The Paα image is the F190N image minus the scaled F187N image and the H$_2$ image is the F215N image minus the scaled F212N image. The archival line emission images were reduced in the same manner and then rotated and shifted to match the new line images. A straight average was taken of the two images for the final line emission images. The F187N image determines the continuum level near the Paα emission to measure the Paα equivalent widths given in Table 2.

The archival wide filter continuum images were also rotated and shifted to match the new images. A median of all the dithered F205W images was produced with no shifts to produce a median sky image. The median sky was then subtracted from the F205W image to remove the thermal sky and instrument background. Contour plots of the ACS UV F140LP image from the data of
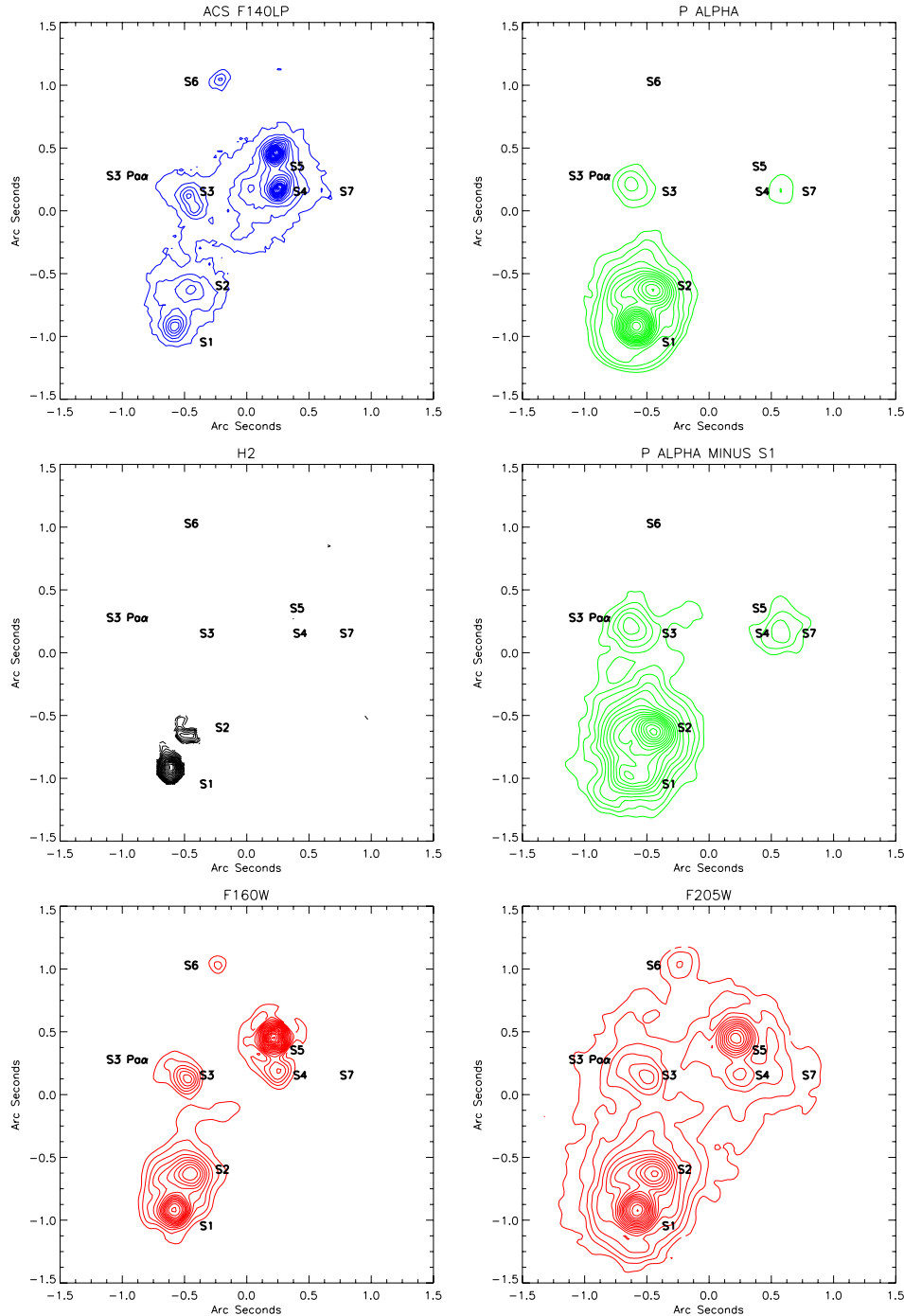
Figure 2. Contour plots of ACS UV, Paα, H₂, and near-IR continuum F160W and F205W images. The plots have a square root stretch. Contour lines do not have the same flux levels between images. The contour plot titled P ALPHA MINUS S1 is the Paα image with the pointlike source S1 subtracted to show the underlying emission. North is up and east is to the left.

(A color version of this figure is available in the online journal.)

Kunth et al. (2004) and of the new NICMOS continuum and line images are shown in Figure 2. Figure 3 shows the images of Paα, H₂, and the F160W continuum, along with ACS UV F140LP image. In these figures, north is up in all cases. Source S8 does not appear in these figures due to the smaller size of the maps and images.

4. SIZES OF THE POINTLIKE SOURCES S1, S5, AND S6

One aspect of SBS0335-052E, as pointed out earlier by Harishita & Hunt (2006), is that the majority of the star formation has occurred in very compact regions rather than being spread diffusely over the region as occurs in the Orion star-forming complex in our own galaxy. Three of the sources S1, S5, and S6 display Airy rings indicative of a point source. We use NICMOS camera 2 observations of known single sources observed to determine the NICMOS camera 2 PSF to get an estimate of the true size of these sources. For the size of the Paα emission, we use the PSF star GD-71 observed in the F190N filter and for the continuum, we use the PSF star HD 3670 observed in F160W filter. The PSF image of GD-71 is a median combination of four images at separate

Table 1
HST Image Observational Parameters

Inst.	Prop.	Mode	Filter	Samp.[a]	NSamp.[a]	Int. Time	Ints.	Total
						s	#	s
NICMOS	10856	Cam. 2	F187N	STEP64	20	768	8	6144
NICMOS	10856	Cam. 2	F190N	STEP32	17	320	8	2560
NICMOS	10856	Cam. 2	F212N	STEP64	20	768	8	6144
NICMOS	10856	Cam. 2	F215N	STEP64	20	768	8	6144
NICMOS	10894	Cam. 2	F187N	STEP16	26	304	16	4864
NICMOS	10894	Cam. 2	F190N	STEP16	25	288	16	4600
NICMOS	10894	Cam. 2	F160W	STEP16	26	304	8	2432
NICMOS	10894	Cam. 2	F205W	STEP64	24	272	8	2176
ACS	10575	WFC1	F550M	⋯	⋯	430	1	430
ACS	10575	WFC1	FR656	⋯	⋯	680	1	680
ACS	9470	SBC	F140LP	⋯	⋯	2700	1	2700

Note. [a] NICMOS only.

positions on the camera 2 detector array. The images were shifted to a common position using IDP3. IDP3 uses bicubic interpolation to resample and shift the images. The HD 3670 PSF image is the addition of two images again shifted and resampled in IDP3. Each of these images was then resampled in an eight times finer pixel scale, again by the bicubic interpolation in IDP3. Moreover, the images of S1, S5, and S6 were resampled in the same way for comparison with the PSF star images.

The two resampled PSF star images were then convolved with 2D Gaussians with FWHM values of 3/8, 5/8, 3/4, and 15/16 of the *original* camera 2 0.″075 pixel size. The radial profiles of the original PSF, the convolved PSF, and the object images at the 8 times finer scale were calculated in IDP3 and then plotted in Figure 4. The convolved radial profiles were visually compared with the source profiles to determine the source size. The comparisons were only made in the inner 0.″15 of the profile to avoid significant contamination from the diffuse background. We did not attempt to subtract the background since it is nonuniform with significant structure, particularly for the Paα background.

The source S1 is resolved in both the continuum and in Paα and is consistent with the radial profile of a Gaussian source with an FWHM of 0.″12–0.″14 convolved with the NICMOS PSF. At the 54.3 Mpc distance of SBS0335-052 (Thuan et al. 1997), the radius of S1, taken as 1/2 of the FWHM of the Gaussian, is between 16 and 18 pc. This is 4 to 5 times larger than the radius of S1 estimated in TSKEV based on the ACS F140LP image.

That estimate was simply done by eye without a similar analysis using convolved PSFs and was clearly an underestimate. This does not, however, alter any of the conclusions in TSKEV, other than the speculation on the formation of intermediate mass black holes. The S1 continuum source may be slightly more compact than the Paschen α, but the difference is less than the error in comparing the observed profile with the broadened PSF profiles. The known "breathing" of the *HST* secondary mirror produces temporal changes of the PSF that are approximately plus and minus half the spacing between the PSF profile and the first broadened profile. The comparison may also be influenced by the extensive diffuse emission in the area. The faint source S6 is also resolved with a size similar to S1 determined in the same manner as for S1.

Source S5 is not resolved in this image. It is consistent with a point source with an upper limit on the radius of 10 pc. It does not have any Paschen-α emission, and is therefore, probably not undergoing intense star formation. All of these sources have sizes consistent with current day globular clusters and are most likely the young predecessors of globular clusters.

5. THE INDIVIDUAL SOURCES IN SBS0335-052E

The sources S1–S7 lie in a roughly north–south alignment with the northernmost source S6 separated from the southernmost source S1 by approximately 1.″9 which is 490 pc at 54.3 Mpc. A supernova cavity lies about 4″ (1 kpc) north of source S1. There appears to be a progression of ages of the clusters along the north–south axis (Thuan et al. 1997; TSKEV) starting with the supernova cavity in the north to the very young sources S1 and S2 which has led to the speculation that the SSCs are the result of triggered star formation propagating from the north to the south (TSKEV). In the following discussion, we have arbitrarily divided the sources into sources with Paα emission and those without. We could have equally well divided the sources into compact (SSCs) and extended. In fact, the compact sources without Paα emission are most likely older versions of the compact sources with Paα emission.

5.1. Sources With Paα Emission

Five sources, S1, S2, S3-Paα, S7, and S8, along with a diffuse background, have detectable Paα emission and, hence, measurable star formation rates. Unlike in TSKEV, the high resolution NICMOS camera 2 images accurately determine the

Table 2
Line Power, $N_e{}^2 V$, and Star Formation Rates

Source	Paα Line Power[a]	$N_e{}^2 V$[b]	Ext. Cor. $N_e{}^2 V$[c]	SFR	Ext. Cor. H$_2$ Pow.	Ext. Cor. H$_2$ Mass	Stellar Mass[d]
	erg s^{-1}	cm^{-3}	cm^{-3}	$M_\odot$ yr^{-1}	erg s^{-1}	$M_\odot$	$M_\odot$
S1	3.4×10^{39}	1.8×10^{65}	7.9×10^{65}	1.2	1.1×10^{38}	21	1.5×10^7
S2	2.5×10^{39}	1.3×10^{65}	5.9×10^{65}	0.9	4.5×10^{37}	8.4	1.1×10^7
S3-Paα	5.3×10^{38}	2.7×10^{64}	1.2×10^{65}	0.18	⋯	⋯	2.3×10^6
S7	3.9×10^{38}	2.0×10^{64}	9.0×10^{64}	0.14	⋯	⋯	9.4×10^4
S8	1.2×10^{38}	6.2×10^{63}	2.8×10^{64}	0.043	⋯	⋯	2.2×10^5
Diffuse	4.9×10^{39}	2.5×10^{65}	5.5×10^{65}	0.85	⋯	⋯	2.05×10^7

Notes.
[a] Assumes a distance of 54.3 Mpc and no correction for extinction.
[b] No correction for extinction.
[c] Assumes Paα extinction by a factor of 4.5 ($A_V = 12.1$ for all sources except for the diffuse emission where it is a factor of 2.25 (see Section 5.1.1).
[d] See Section 7 for the calculation of the stellar mass.

Table 3
Observed Line and Continuum Measurements[a]

Source	Paα erg s^{-1} cm^{-2}	H$_2$ erg s^{-1} cm^{-2}	0.14 μm Jy	1.6 μm Jy	2.05 μm Jy	Paα Equivalent Width Å
S1	9.7×10^{-15}	8.8×10^{-17}	1.7×10^{-5}	2.6×10^{-5}	4.5×10^{-5}	1281
S2	7.2×10^{-15}	3.5×10^{-17}	8.6×10^{-6}	2.3×10^{-5}	3.5×10^{-5}	1182
S3-Paα	1.5×10^{-15}	⋯	1.2×10^{-5}	1.9×10^{-6}	1.1×10^{-5}	1103
S3	⋯	⋯	1.2×10^{-5}	1.1×10^{-5}	5.9×10^{-6}	⋯
S4	⋯	⋯	4.1×10^{-5}	1.2×10^{-5}	9.2×10^{-6}	⋯
S5	⋯	⋯	4.9×10^{-5}	2.4×10^{-5}	1.9×10^{-5}	⋯
S6	⋯	⋯	4.1×10^{-6}	4.1×10^{-6}	3.4×10^{-6}	⋯
S7	1.1×10^{-15}	⋯	6.0×10^{-7}	3.7×10^{-6}	4.3×10^{-6}	3478
S8	3.4×10^{-16}	⋯	1.2×10^{-6}	1.2×10^{-6}	1.6×10^{-6}	2079
diffuse	1.37×10^{-14}	⋯	5.7×10^{-4}	2.6×10^{-5}	2.1×10^{-5}	672

Note. [a]All fluxes are for an aperture diameter of 5 pixels (0″.378) and the equivalent widths are for an aperture diameter of 6 pixels (0″.454). The flux and equivalent width errors are estimated as 10% and are dominated by the amount of extended flux.
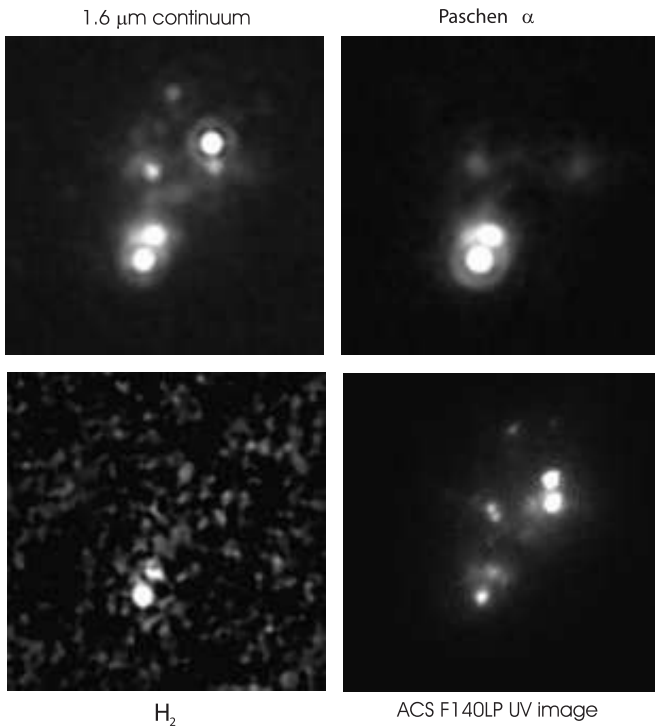

Figure 3. Linear stretch 40 × 40 pixel NICMOS camera 2 images of SBS0335-052 in the continuum, Paα, H$_2$, and the ACS F140LP UV image. The images are approximately 3″ on a side. Note the Airy rings around S1, S5, and S6 (faint) in the 1.6 μm continuum image and around S1 in the Paα image. North is up and east is to the left.

distribution of Paα flux between S1 and S2. In addition to the Paα flux associated with the continuum emission of S1 and S2, the images also show diffuse background Paα emission in the region of S1 and S2, which was not evident in the previous lower spatial resolution observations. The total diffuse Paα flux is comparable to the sum of the fluxes from the sources and is due to either in situ ionizing stars or to ionizing radiation that has leaked from the sources S1 and S2. The former is more likely than the latter (see Section 5.1.2). If the emission is due to ionization by in situ stars, it is not clear whether it is due to a diffuse distribution of individual stars or a distribution of smaller clusters that is not resolved in the present observations.

Two types of photometry were carried out on the sources. The first is an aperture photometry with a 5 pixel diameter (0″.378) that encompasses all of the flux inside the first Airy ring of a point source. This is 74% of the total flux of a point source in the F160W filter and 69% in the F190N filter. Larger apertures begin to infringe on adjacent sources. To first-order adjacent sources add approximately the same flux to the aperture as falls outside the aperture from the primary sources. We, therefore, do not correct the aperture flux for the percentage of primary object flux in the aperture. The background was measured in annular rings 3 pixels thick around the sources. The inner and outer diameters of the annular rings were adjusted to avoid flux from adjacent sources. The measured backgrounds, adjusted to the area of the photometric aperture, were subtracted from the source flux. The photometric error is taken as 10% of the total flux for the bright compact sources and is dominated by the systematics of source overlap and background subtraction.

The equivalent widths were similarly measured in a 6 pixel (0″.454) diameter aperture. The continuum measure for the equivalent widths is provided by the narrow band F187N filter which is adjacent to the F190N band that measures the Paα flux. This filter accurately measures the continuum level at the location of the Paα line and is free of other contaminating emission lines. The larger aperture was used to increase the signal to noise of the measurements in the F187N filter which has much lower flux than the Paα filter or the broadband F160W filter. The smaller aperture photometry agreed within their signal-to-noise ratios with the larger aperture measurements. Table 3 gives the line and continuum fluxes for all of the sources along with the equivalent widths of the Paα line. It is evident that the equivalent widths of the extended sources S7 and S8 are significantly higher than for the compact sources S1 and S2. Again note that S7 is the source denoted by a question mark in TSKEV and S8 is the source marked S7 in Papaderos et al. (2006). Unlike in TSKEV, the new observations are deep enough to detect the faint continuum associated with the extended sources and are of high enough resolution to discern the offset between the continuum and line emission in S3. In the following, we discuss the nature of the sources.

5.1.1. Sources S1 and S2

The Paα emission in S1 and S2 is coincident with the continuum emission. In the new images, it is clear that the Paα emission in the region of S1 and S2 has at least three components, S1, S2, and diffuse; therefore, the extinction of $A_V = 12.1$ derived from the comparison of Paα and Brα flux ratios in TSKEV is an average extinction. The extinction curves of Rieke & Lebofsky (1985) were used to compute the
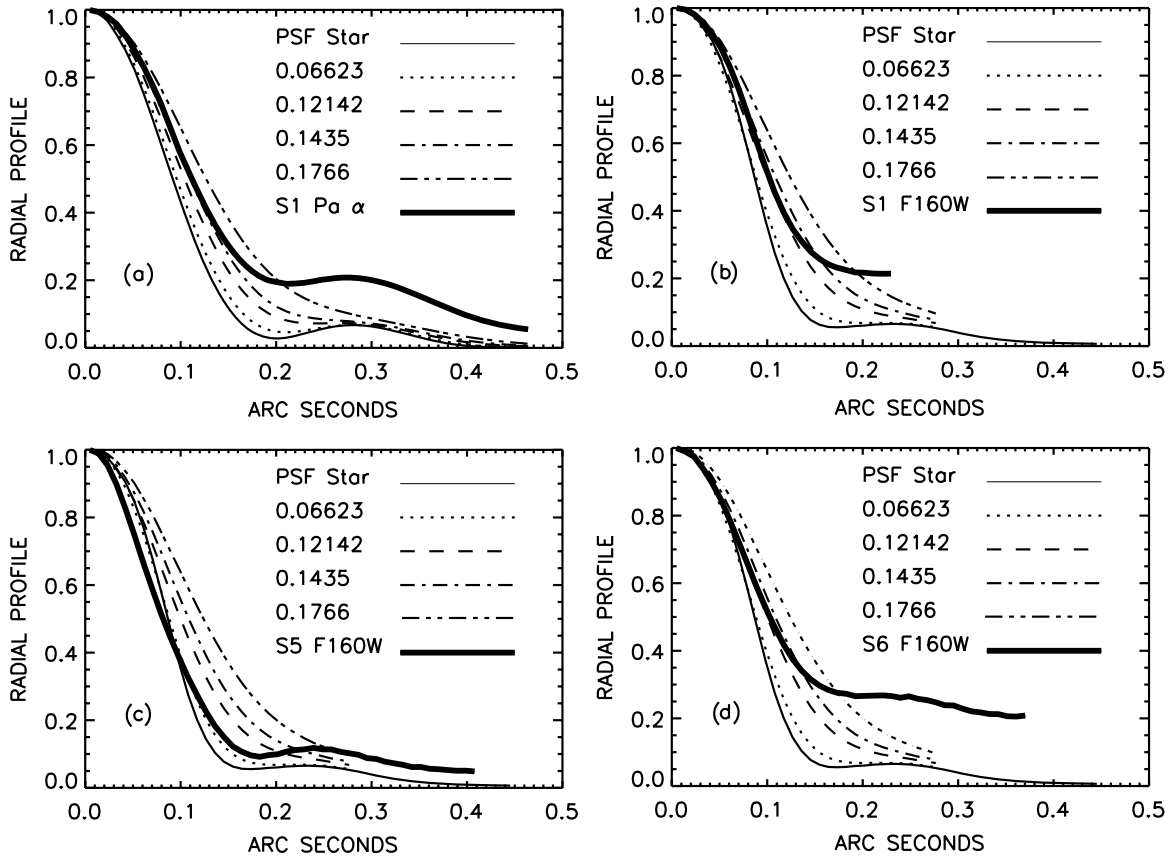
Figure 4. Radial profile of (a) the Paschen-α emission (F190N filter) from source S1 and the F160W continuum profiles of (b) S1, (c) S5, and (d) S6 compared to the radial profiles of a standard PSF star and that star convolved with Gaussian profiles with the FWHM values listed in the legend. The values correspond to 3/8, 5/8, 3/4, and 15/16 of a pixel, respectively. The profiles do not correspond to the PSF profiles in the regions beyond 0″.15 due to diffuse emission or adjacent sources. See the text for a discussion of the source sizes. The names of the sources appear in the last row of the figure legends.

extinction. The extinction for any of the individual components may be different than the average. If, however, the extinction is primarily foreground, then the extinction affects all sources equally and the derivation is valid. We note that the 1.6–2.05 μm color is similar for S1 and S2 indicating that they may have the same extinction. The color of the diffuse continuum emission is blue rather than red, which supports the idea of less extinction in the regions of diffuse emission.

To get an estimate of the spatial distribution of the extinction, we produced an Hα image from the archive ACS *HST* images of SBS0335-052 from Proposal 10575 (PI G. Östlin) by subtracting the F550M image from the FR675N ramp filter image. The F550M image was multiplied by a factor of 0.2 to account for the differences in throughput. The factor was determined by the requirement that the sources with no Paα emission, and therefore presumed to have no Hα emission, subtract to zero. This does not guarantee an accurate subtraction in the sources with hydrogen line emission since they are generally redder than the nonemission line sources. The Hα image was then resampled to the spatial resolution of the NICMOS Paα image. The ratio of the two images is an indicator of the relative extinction and is scaled to unity at the location of S1. The difference in wavelength, which changes the diameter of the Airy rings, limits the accuracy of this procedure. The extinctions of S1 and S2 are equal within the signal to noise of the image. The extinction of the extended sources S3-Paα, S7, and S8 are also equal to S1 and S2 within the rather low signal to noise. The extinction in the diffuse region is 1/2 of that of S1 and S2 in terms of absolute flux. We, therefore, decrease the extinction in the dif-

fuse flux by a factor of two in computing the properties of the diffuse emission. The extinction map shows significant structure due to the differences in spatial resolution, and we estimate the accuracy of the relative extinctions derived from the map to be 20%.

The volume emission measure ($N_e^2 V$) for S1 of 7.9×10^{65} cm^{-3} is almost exactly the same as the previous measurement in TSKEV of 7.2×10^{65}; therefore, the primary conclusions on the nature of S1 remain valid. Note that throughout the discussion of the Paα sources, the ionized gas temperature is assumed to be 20,000 K as discussed in TSKEV. S1 has a stellar mass of 1.5×10^7 $M_\odot$ (see Section 7) with stars of less than 1 $M_\odot$ probably not yet on the main sequence. There are 8650 stars earlier than O9 and the luminosity of the stellar population is 3.4×10^9 $L_\odot$ based on the output of Starburst99 (Leitherer et al. 1999) if we only account for the Paα flux in the pointlike object. A further discussion of the Starburst99 calculation is given in Section 6. The star formation rate is 1.2 $M_\odot$ yr^{-1} based on a Case B recombination rate for 20,000 K (Osterbrock 1989) and the SFR to Q(H^0) ratio given by Kennicutt (1998). The specific star formation rate, i.e., the star formation rate divided by the mass of the S1, of 1.4×10^{-7} yr^{-1} is relatively high. However, the specific star formation rate for the entire galaxy of 3.7×10^{-9} yr^{-1} is quite low.

We now resolve S2 from S1 and obtain a volume emission measure of 5.9×10^{65} cm^{-3} for S2, somewhat less than the arbitrary half of the total S1 plus S2 emission measure that was assigned to S2 in TSKEV. The parameters discussed above for S1 simply scale for S2 by the ratio of the volume emission

measures. The difference between the values of the emission measure for S1 plus S2 in this work versus TSKEV is due to the separation of the sources from the diffuse background, some of which was included in the aperture measurement of Paα in the previous work. Unlike S1, S2 is clearly not a pointlike object. It is irregular in shape and extended in the east–west direction. Its average spatial extent is $0\farcs05$ larger than S1 which puts its radius at 30 pc averaged over the east–west and north–south directions.

5.1.2. Diffuse Emission Around S1 and S2

The diffuse emission is the Paα emission that remains after all of the emission associated with the sources S1–S8 is subtracted. The associated diffuse continuum emission is defined in the same way. The majority of the diffuse emission, defined in this manner, is in the region around S1 and S2. In the commonly used radio emission measure, the volume emission measure of 5.5×10^{65} cm^{-3} is equivalent to that of 1.2×10^4 O7 stars. The volume emission measure of the diffuse emission is more than 1/3 of the emission measures of S1 and S2. This implies that the current star formation is roughly equally spread between diffuse and compact regions. We consider two possible interpretations of the diffuse Paα emission. The first is ionizing radiation from S1 and S2 that escapes the clusters and ionizes the surrounding gas. The second is an underlying population of young stars.

The volume emission measure of the diffuse gas is 40% of the volume emission measure of S1 and S2. The diffuse emission therefore requires some source of ionizing flux at the level of 40% of that produced by S1 and S2. This assumes that all of the ionizing photons from the source of ionizing flux for the diffuse emission are absorbed by the diffuse gas and none escape from the region. If the source of ionizing photons is photons that escape S1 and S2 but are trapped by the diffuse gas, the mass and luminosity of the two sources must increase by a similar percentage. This would place the mass of S1 and S2 at 2.1×10^7 $M_\odot$ and 1.6×10^7 $M_\odot$, respectively. The luminosities for S1 and S2 become 4.8×10^9 $L_\odot$ and 3.5×10^9 $L_\odot$. These are still reasonable parameters for the two SSCs, but they lie at the high side of known clusters (Zhang & Fall 1999; Dowell et al. 2008). A difficulty may be that this makes the percentage of dust re-emitted luminosity of 1.2×10^8 $L_\odot$ (Houck et al. 2004; Engelbracht et al. 2008), only 20% of the total luminosity of S1 and S2. The discussion of the H$_2$ emission in Section 8, however, shows that this is a reasonable number. Another difficulty could arise if the assumption that all of the ionizing flux produces observable Paα emission is false. If a large fraction of the ionizing flux escapes the region, then the mass and luminosity requirement can become unrealistic. Also, if the diffuse emission is simply ionized gas with no stellar continuum, its Paα equivalent width should be higher than that of S1 and S2, instead it is lower. The equivalent width calculations described in Section 6 in fact show that the diffuse emission has the lowest equivalent width of any Paα source. This is very strong evidence against the concept that the diffuse Paα is due to UV leakage from the clusters. The discussion in Section 6 also indicates that the diffuse emission stellar population is most likely older than the other Paα sources.

The possibility that the diffuse ionization region is produced by an in situ diffuse distribution of stars is a more plausible explanation. Accounting for the diffuse emission with in situ stars requires a stellar mass of 40% of the combined masses of S1 and S2 if the stars are at the same epoch of evolution as the two SSCs. The net star formation rate of the diffuse

component in this explanation is 0.85 $M_\odot$ yr^{-1}. If this is the correct explanation for the diffuse emission, then star formation in SBS0335-052 is occurring in a bimodal fashion. The majority of the stellar mass is in the form of compact objects, S1–S6, but the current star formation is roughly divided 2 to 1 between the compact and diffuse regions, whereas the current star formation in the Milky Way appears to be predominantly in diffuse regions.

5.1.3. Source S3-Paα

S3-Paα is a source with a Paα equivalent width very close to those of S1 and S2. To delineate the Paα emitting region from the continuum source S3, we have designated the emission region S3-Paα. The separation of S3-Paα (from the adjacent continuum source as shown in Figure 5) is the reason that Papaderos et al. (2006) found an offset between the continuum and the line emission near S3. As with the diffuse emission, the question is whether this is a separate star-forming source or is it a gas that is ionized by the double source S3 or possibly the more distant sources S1 and S2. S3-Paα has a volume emission measure of 2.8×10^{64} cm^{-3} which is equal to that of 2.9×10^3 O7 stars. If this volume emission measure is due to sources other than in situ stars, it would have to be due to intercepted ionizing flux from one of the other sources.

The lack of detectable Paα flux at the location of S3 argues against it as the source of the ionizing flux. The only possibility would be if the region around and in S3 is largely free of gas. The observed Paα region subtends 2.2 steradians as seen from the location of S3 if its radial dimension is the same as its extent on the sky and, therefore, receives approximately 17% of the emitted flux from S3 if it is emitted isotropically. Note that as in the discussion of the diffuse emission, we assume that the source of UV flux, the stars, emit radiation isotropically. Sources can be "beamed" by large-scale distributions of dust but dust structures simply block ionizing flux, and do not enhance the flux along any particular line of sight. The volume emission measure for S3 would then have to be 7.6×10^{65} cm^{-3}, almost as high as S1. The requirements for ionization by S1 and S2 are even more formidable. S3-Paα subtends 3.4×10^{-2} steradians as seen from S1. The ionizing flux from S1 and S2 would then have to be 370 times larger than listed in Table 2, increasing their stellar mass to almost 10^{10} $M_\odot$. This is clearly not possible.

The most likely source of ionization of S3-Paα is in situ young stars. This is the explanation that requires the minimum amount of ionizing flux as is the case for the diffuse flux discussed earlier. The star formation in this source is in a more extended region than in the SSCs, again showing the bimodal nature of high pressure, low metallicity star formation. Another argument in favor of local star formation in S3-Paα is that the equivalent width of the Paα flux is almost exactly the same as in S1 and S2. This argues that S3-Paα is the location of early star formation such as in S1 and S2, while the diffuse emission around S1 and S2, which has a lower equivalent width, is due to an older stage of star formation as is further discussed in Section 6.

5.1.4. Sources S7 and S8

Two of the Paα emitting sources are distinguished by significantly larger equivalent widths than the rest of the sources. They are S7, the previously known source that was marked with a question mark in TSKEV and S8, $2\farcs59$ (664 pc) from S1 as shown in Figure 1. Note that both S7 and S8 are clearly visible in the images presented in their Figure 3 by Östlin et al. (2008), but were not commented on in the paper. Both of these sources are extended and are far away from any other known

ionizing sources, particularly for S8. It appears clear that these must be sites of new star formation and the ionization is due to in situ stars. Their volume emission measures, as shown in Table 2, are about a factor of 10 less than S1 and S2, and the total mass of stars is less. The star formation rates are 0.14 and 0.043 $M_\odot$ yr^{-1}, respectively. The extinction map discussed in Section 5.1.1 gives the same average extinction in S7 and S8 as for S1 and S2, but the low signal to noise of the continuum make variations by a factor of 2 quite possible.

5.2. Sources S3, S4, S5, and S6

The sources S3, S4, S5, and S6 are distinguished by the absence of any associated Paα emission indicating a lack of ionized gas and current star formation in these sources. Their continuum 1.6–2.05 μm colors are bluer than S1 and S2 which is most likely a function of the foreground extinction rather than their intrinsic color. Source S3 deserves special mention as it may be the most enigmatic of all the non-Paα sources. In the ACS UV F140LP image in Figure 3, S3 is clearly double, also seen in Figure 1 right of TSKEV, with a spacing of 0''08 (23 pc) in the northeast–southwest direction on the sky. The infrared continuum is centered on the northeast component with no indication of a southwest source or extension. The continuum fluxes for S3 are also hard to explain. At UV wavelengths, the two components of S3 are roughly equal in brightness (Figure 3, ACS UV F140LP), while at infrared wavelengths (Figure 3, 1.6 μm continuum) only the northeast component is seen but it is quite bright. A possibility is that the northeast component has an intrinsic brightness much brighter than the southwest, but is much more heavily obscured so that at UV wavelengths they appear to be of roughly the same brightness. This explanation is possible but appears to be a bit contrived. The obscuring dust would have to be at a significant distance in front of the northeast component of S3, otherwise we should see mid- and far-infrared emission from that location. On the other hand, it must be small enough to obscure only the northeast source.

The discussion in Section 6 indicates that the non-Paα sources are older than the other sources which is consistent with triggered star formation starting in the north and propagating southward. Only S3 is inconsistent with this progression since it is very near the young star-forming region S3-Paα. S5 is somewhat unique in that it is extremely compact as discussed in Section 4. S5 could possibly be a young globular cluster that has undergone core collapse. All of the non-Paα sources have probably had most of the residual gas swept out of them and are bound young globular clusters.

6. THE AGES OF THE SOURCES

Table 3 gives equivalent widths for the Paα emission sources. The equivalent width is relative to the continuum measured in the F187N narrow line filter which is adjacent in wavelength to the F190N filter that measures the Paα flux. Use of the F160W or F205W filter images would give a higher signal to noise but the uncertainty in the detailed spectrum and the inclusion of other emission lines in the broad filter compromises the accuracy of the equivalent width. In an attempt to determine the ages of the emission line sources, we ran a Starburst99 (Leitherer et al. 1999) simulation with a stellar mass range of 0.1–120 $M_\odot$, a standard Kroupa IMF, a metallicity of 0.001, time steps of 10^5 yr, and an instantaneous burst of star formation. The luminosity of the Paα line was calculated from the output Paβ luminosity using a Case B recombination and a temperature
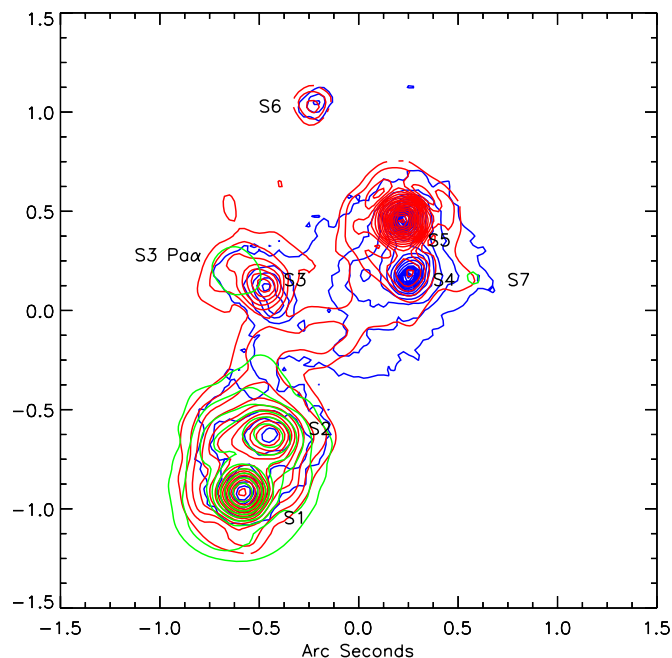

Figure 5. Combined contours of the ACS UV emission (blue), near-IR continuum (red), and Paα (green). Note the relative offsets of the UV continuum, near-IR continuum, and Paα for the source S3. North is up and east is to the left.

(A color version of this figure is available in the online journal.)

of 20,000 K. From this line luminosity and the computed continuum flux at the wavelength of Paα, the equivalent width of Paα was calculated and plotted against age in Figure 6. Note that the continuum includes both stellar and nebular emission. The plot is marked with asterisks at the equivalent width appropriate for each source. The position marked for S8 is at the oldest consistent time. This equivalent width is achieved at two earlier times, but the time spent at those values is very brief, 10^5 and 1.5×10^5 yr, as opposed to 1.3×10^6 yr at the marked position. The dip in equivalent width around 4×10^6 yr is due to a rise in the infrared continuum rather than a dip in the Paα luminosity.

The parameters of the Starburst99 simulation have little effect on the age sequence and ages of the sources for an instantaneous starburst. It is only the lifetimes of the high mass stars that affect the evolution of the ionizing flux. Higher metallicities would decrease the ionizing flux per unit mass and different IMFs would change the total mass needed to achieve the observed ionizing fluxes but not the time evolution. To check this assumption, we produced another Starburst99 simulation with a Salpeter rather than Kroupa IMF. The resultant equivalent to Figure 6 was indistinguishable from Figure 6. These changes only affect the mass estimate discussed in Section 7. If, however, the star formation in each of the clusters is not short relative to the present age of the cluster, the ages could be quite different from those derived here. The ages from Figure 6 are only valid if the star formation epoch is short relative to the age of the clusters.

Figure 6 indicates that S7 and S8 are young star-forming regions with ages less than 10 million years with S7, the youngest, at about 4 million years. S1, S2, and S3-Paα all formed at roughly the same epoch and are now about 10 million years old. The diffuse emission is from an older group of stars formed a million years before the S1, S2, S3-Paα group. The sources without detectable Paα emission are at least 15 million years old or older. This shows a general progression in age of the SSCs with oldest sources in the north and the youngest in the
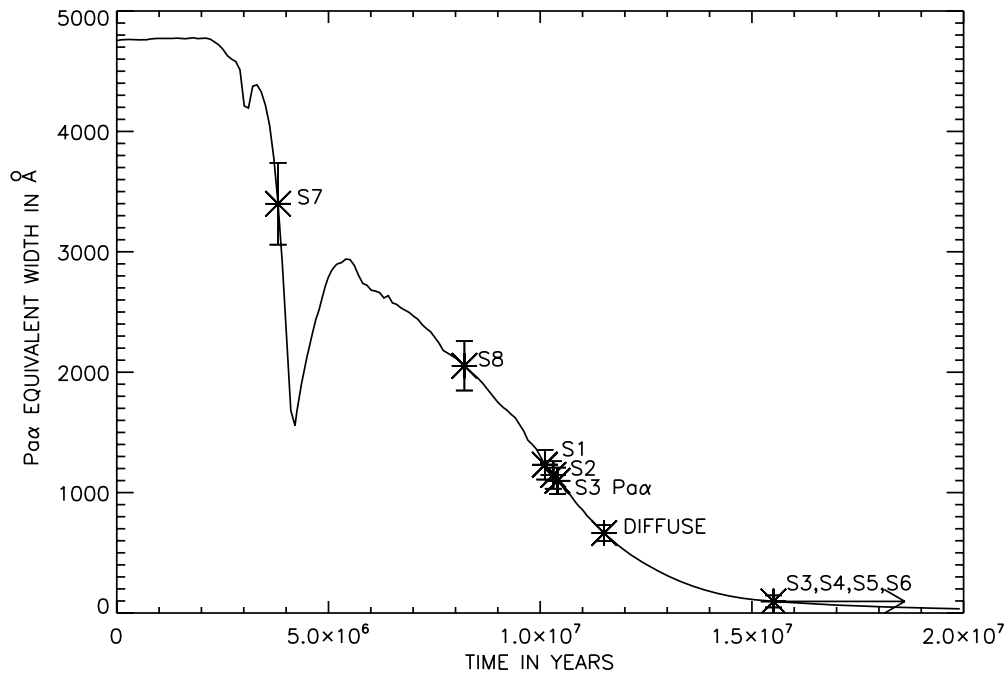
Figure 6. Solid line represents the equivalent width of Paα vs. time calculated from a Starburst99 simulation. The asterisks are placed on this line at the location of the equivalent widths measured for each source. The location of the position of the S8 equivalent width is at the longest time since the simulated galaxy spends very little time at the same value of the equivalent width that is achieved at two earlier times. The dip in equivalent width at about 4×10^6 yr is due to an increase in continuum flux rather than a decrease in line emission. It marks the brightest continuum epoch of the cluster.

south, evidence for triggered star formation running from north to south. A new star formation is now occurring in S7 and the more distant S8. A 1 km s^{-1} wind would propagate 10 pc in 10 million years which makes it doubtful that S8, which is 340 pc from S1 and S2, is causally affected by the SSCs.

7. STELLAR MASSES

The Starburst99 output provides an estimate of the stellar mass for those objects with Paα emission. The Starburst99 calculation used a stellar mass of $10^8 M_\odot$; therefore, the ratio of the observed Paα power versus the calculated Paα power times $10^8 M_\odot$ at the age given in Figure 6 gives the mass. The masses are given in the last column of Table 2. As discussed in Section 6, the masses are sensitive to the parameters used in the Starburst99 model, particularly on the IMF and metallicity used. The metallicity is appropriate for that measured in the clusters but we do not have sufficient information to accurately determine the actual IMF and many of the low mass stars are still probably in their premain sequence evolutionary stages. The largest mass components are the two compact sources S1 and S2 plus the diffuse component which total to a mass of $4.65 \times 10^7 M_\odot$. If the SSCs with no Paα are included with an average mass of $10^7 M_\odot$ per SSC, then the total mass is on the order of $8 \times 10^7 M_\odot$. Taking the total gas mass as $2.1 \times 10^9 M_\odot$ (Pustilnik et al. 2001), the ratio of total stellar mass in the nucleus of SBS0335-052E to the gas mass of 1 to 26 is significantly higher than the average nuclear cluster mass-to-gas ratio found by Seth et al. (2008). The average nuclear cluster mass-to-gas ratio in Seth et al. (2008), however, is dominated by nuclear clusters in large spiral galaxies rather than in BCD low metallicity galaxies. The objects S3-Paα, S7, and S8, which have less concentrated star formation, have significantly less mass, with S7 having only $9.4 \times 10^4 M_\odot$. This may represent star formation in what we would term open clusters and they may not remain bound for very long.

8. H$_2$ EMISSION IN S1 AND S2

A new finding of this investigation is the precise location of the H$_2$ emission in S1 and S2. Previous ground-based observations by Vanzi et al. (2000) did not have the spatial resolution to resolve the sources. The contour map in Figure 7 shows separate emission regions in both S1 and S2. The emission region in S1 is consistent with being pointlike, while the emission in S2 is extended as is the continuum emission. Both of the regions are offset from the center of the continuum emission. The H$_2$ emission region in S1 is offset by 0″.04 (11.6 pc) to the east from the continuum center, and the H$_2$ region in S2 is offset by the same amount to the south. These offsets are less than the radii of the clusters so that the molecular emission regions exist inside the region of Paα emission. There is no chance that the offsets are due to misalignment of the images as the new H$_2$ and Paα images were taken in the same orbit for each dither position with no change is *HST* attitude. Taken alone, these images clearly show the offset. The additional archival Paα images were then registered to the new Paα images and the same offset was present. It is remotely possible that the two H$_2$ regions are located along the line of sight to S1 and S2, but outside of the clusters. This might be considered a possibility if only one SSC coincided with an H$_2$ source, but it is highly unlikely that two SSCs lie along the line of sight to the only two H$_2$ sources.

The survival of a molecular gas inside the sources is another line of evidence that the photoionizing flux does not reach throughout the clusters. The molecular regions are also the most likely sources of the observed mid-infrared emission found by Houck et al. (2004) and further discussed by Engelbracht et al. (2008). If these are the emission regions and they are small dust regions embedded in the cluster, then they are not capable of absorbing all of the luminosity of the cluster and re-emitting it in the infrared. This accounts for the low IR luminosity to total luminosity ratio discussed in Section 5.1.2. Their location inside
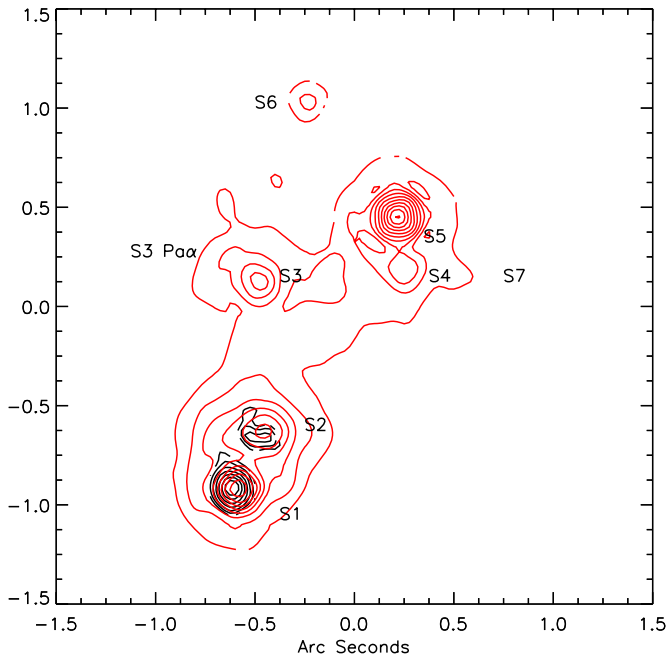
Figure 7. Near-IR continuum contours (red) and H_2 emission (black). Note the slight offset of the H_2 emission to the east of the near-IR continuum for S1 and to the south for S2. North is up and east is to the left.

(A color version of this figure is available in the online journal.)

the cluster also probably accounts for the high temperature of the observed dust emission.

The calculation of the mass of H_2 needed to produce the observed emission depends on the temperature of the H_2 gas and the ratio of thermal to fluorescent emission, neither of which is accurately available. Vanzi et al. (2000) find that the emission is a mixture of fluorescent and thermal emission which makes the line ratios an unreliable monitor of the thermal temperature. To get a rough estimate of the amount of H_2 needed to produce the observed (1-0) S(1) emission, we calculate the H_2 abundance needed for a 2500 K thermal gas using an Einstein A value of 3.471×10^{-7} s^{-1} (Wolniewicz et al. 1998). This estimate should be good to about a factor of two to three, modulo the amount of extinction, if the contributions from thermal and fluorescent emission are about equal. Table 2 gives the mass of H_2 needed to produce the observed line strength under the assumption of the same extinction as used in the Paα calculation. This is a lower limit on the H_2 since the extinction will be significantly higher in the dust-protected molecular region. Houck et al. (2004) calculate a 9.7 μm extinction of 0.49 mag which predicts about 2.6 mag of extinction at 2.12 μm as opposed to the 1.4 mag derived from the atomic hydrogen lines. Vanzi et al. (2000) spectroscopically observed a line strength that is about 2.2 times larger than that quoted in the table. We may have missed some of the extended flux, but the value here is within 1.9σ of the spectroscopic value.

9. EVOLUTION AND FEEDBACK IN SBS0335-052E

The primary conclusions on the nature of the SSCs S1 and S2 in TSKEV remain intact. Although the possibility exists that the diffuse emission around S1 and S2 is due to ionizing radiation from them, the more likely explanation is that the ionization is done by in situ stars. The lower equivalent width of the diffuse radiation is strong evidence for this view. If the diffuse emission was due to pure ionized gas with no stars, its

equivalent width should be higher rather than lower than the equivalent width of the star-rich clusters S1 and S2. This leaves the conclusion that S1 and S2 are currently not producing any negative feedback from photoionizing flux on star formation in SBS0335-052E intact. The delay in photoionizing feedback may also have implications for planet formation. The ambient UV radiation field may be significantly less than the fields calculated without considering absorption by stellar winds (Fatuzzo & Adams 2008). This would increase the probability of planet formation even in the environment of an SSC which would normally be considered not conducive to planet formation. It also has implications on whether globular clusters are good sites for future searches for planets.

The deeper and higher spatial resolution images have revealed that there are star formation regions in SBS0335-052E that are not compact SSCs. Two of these regions, S7 and S8, appear to be younger than S1 and S2, while the other extended region, S3-Paα, appears to be roughly coeval with S1 and S2. The appearance of these extended regions of star formation may mark the end of the formation of compact stellar clusters and perhaps the beginning of a negative photoionizing feedback. Because the volume emission measures of the extended sources are significantly lower than that of S1 and S2, modulo extinction, they do not contribute much to the net radio emission. If the extended regions have extended HII regions, then they should be optically thin. Future observations with the EVLA should be capable of taking spatially resolved radio images of the different sources to determine whether they are optically thick or thin at radio frequencies.

Elmegreen & Efremov (1997) discuss the effect of pressure on the ratio of compact to diffuse star formation. They claim that high pressure favors the formation of compact clusters as opposed to diffuse star formation. Bekki (2008) has simulated the merger of two dwarf galaxies with stellar masses $4 \times 10^8 M_\odot$ and gas masses of $8 \times 10^8 M_\odot$. Twenty-two percent of the new stars in this simulation appear in compact clusters, far more than in simulations at lower pressures. SBS0335-052 has a gas mass of $2.1 \times 10^9 M_\odot$ and a gas-to-stellar mass ratio of 25–26 (Pustilnik et al. 2001; this work); therefore, the central gas pressure should be significantly higher than the model considered by Bekki (2008) leading to an increased fraction of star formation in clusters.

10. COMPARISON WITH OTHER RECENT WORK

One day after the initial submission of this manuscript, new work on SBS0335-052E became publicly available—Reines et al. (2008), hereinafter RJH, which reaches to some different conclusions than this work. RJH derive significantly lower masses and ionizing fluxes than this work, particularly for the youngest sources, S1 and S2, where the difference is a factor of 15 and 10, respectively. The main diagnostic tool of RJH is SED fitting to the optically observed *HST*/ACS images of Östlin et al. (2008). This fitting, confined to the first four ACS bands, leads to significantly lower dust extinction values than are derived in this work and TSKEV. Our A_V value is 12.1 as opposed to 0.5 in RJH. This is the primary reason for the different conclusions drawn between the two works. Source fluxes redder than the F550M band deviate strongly from the RJH-derived SED and must be explained by a combination of hot dust and extended red emission (Witt & Vijh 2004). The extinction model needed to account for the observed hydrogen emission line ratios is gray from Hβ to Brγ with 0.9 mag of extinction for each line. Our model with an A_V value of 12.1 and an extinction law given by

Rieke & Lebofsky ([1985](#)) implies significantly more line flux which requires a larger $N_e^2 V$ and more mass in stars to provide the ionizing flux. This model does not require the extra emission components to match the observed fluxes.

11. SUMMARY

The new high spatial resolution NICMOS camera 2 images of the region of SBS0335-052E that contains a compact group of SSCs have improved our detailed knowledge of the geometry and physics of the system. There are six pointlike objects, seven if the binary nature of S3 is taken into account, that are either currently SSCs (S1 and S2) or were most likely previously SSCs (S3–S6). We now know that the continuum source S3 is not at the same position as the Paα source S3-Paα. In addition to the compact sources, there are four diffuse or extended regions of Paα emission, indicating current star formation in noncompact objects. It should be noted, however, that a diffuse distribution of many compact sources with stellar masses on the order of $10^4\,M_\odot$ would be difficult to differentiate from a diffuse distribution of individual stars. Two of these regions, S7 and S8, appear to be significantly younger than the two star-forming SSCs. One of the star-forming regions, S8, is well separated from the compact group of previously known sources. These regions are the first indication of a significant star-forming activity in SBS0335-052E in anything other than very compact clusters. They are significantly less massive than the very compact clusters, modulo extinction, and may be open clusters that will not remain bound after the gas is expelled. The new images still support the general picture of delayed photoionizing negative feedback from the sources S1 and S2 along with the general picture of propagating star formation from the north to the south. This delay in feedback may also affect the number of planetary systems that can form in what would normally be considered a very harsh environment. We have also confirmed that the H$_2$ emission is inside both S1 and S2, but is not at the exact center of the two objects and probably marks the location of the regions producing the observed mid-infrared emission.

One result that differed from TSKEV is the size of S1 where the possibility was raised that SSCs may be the origin of intermediate mass black holes through the merging of stellar mass black holes created by supernova events in the cluster. The new radius of 15 pc is approximately 3 times larger than the previous radius and would affect the possibility of forming intermediate mass black holes. Equation (1) of Zwart et al. ([2006](#)) indicates that the timescale for forming merged intermediate mass black holes is dependent on radius to the 3/2 power. The new radius of S1 would therefore increase the timescale by about a factor of 5. Even at the new radius, however, SSCs seem to be a leading candidate for the formation

site of greater than stellar mass black holes. See also the very recent discussion on massive black hole formation in early low metallicity star clusters by Devecchi & Volonteri ([2008](#)).

REFERENCES

Bekki, K. 2008, MNRAS, 388, L10
Devecchi, B., & Volonteri, M. 2008, arXiv:0810.1057v1
Dowell, J. D., Buckalew, B. A., & Tan, J. C. 2008, AJ, 135, 823
Elmegreen, B. G., & Efremov, Y. N. 1997, ApJ, 480, 235
Engelbracht, C. W., Rieke, G. H., Gordon, K. D., Smith, J.-D. T., Werner, M. W., Moustakas, J., Wilmer, C. N. A., & Vanzi, L. 2008, ApJ, 678, 804
Fatuzzo, M., & Adams, F. 2008, ApJ, 675, 1361
Harishita, H., & Hunt, L. K. 2006, A&A, 460, 67
Houck, J. R., et al. 2004, ApJS, 154, 211
Izotov, Y. I., Lipovetsky, V. A., Chaffee, F. H., Foltz, C. B., Guseva, N. G., & Kniazev, A. Y. 1997, ApJ, 476, 698
Izotov, Y. I., & Thuan, T. X. 2007, ApJ, 665, 1115
Kennicutt, R. C., Jr. 1998, ARA&A, 36, 189
Kennicutt, R. C., Jr., et al. 2003, PASP, 115, 928
Kunth, D., Hayes, M., Östlin, G., Mas-Hesse, J. M., Leitherer, C., & Petrosian, A. 2004, arXiv:astro-ph/0407584v1
Kunth, D., Leitherer, C., Mas-Hesse, J. M., Östlin, G., & Petrosian, A. 2003, ApJ, 597, 263
Leitherer, et al. 1999, ApJS, 123, 3
Lytle, D., Stobie, E., Ferro, A., & Barg, I. 1999, in ASP Conf. Ser. 172, Astronomical Data Analysis Software and Systems VIII, ed. D. Mheringer, R. Plante, & D. Roberts (San Francisco, CA: ASP), 445
Osterbrock, D. E. 1989, in Astrophysics of Gaseous Nebulae and Active Galactic Nuclei (Mill Valley, CA: Univ. Science Books)
Östlin, G., Hayes, M., Kunth, D., Mas-Hesse, J. M., Leitherer, C., Petrosian, A., & Atek, H. 2008, arXiv:astro-ph0803.1174v3
Papaderos, P., Izotov, Y. I., Guseva, N. G., Thuan, T. X., & Fricke, K. J. 2006, A&A, 454, 119
Pustilnik, S. A., Brinks, E, Thuan, T. X., Lipovetsky, V. A., & Izotov, Y. I. 2001, AJ, 121, 1413
Reines, A. E., Johnson, K E., & Hunt, L. K. 2008, AJ, 136, 1415
Rieke, G. H., & Lebofsky, M. J. 1985, ApJ, 288, 618
Seth, A., Agüeros, M., Lee, D., & Basu-Zych, 2008, ApJ, 678, 116
Thompson, R. I., et al. 2005, AJ, 130, 1
Thompson, R. I., Sauvage, M., Kennicutt, R. C., & Engelbracht, C. W. 2006, ApJ, 638, 176, (TSKEV)
Thuan, T. X., Izotov, Y. I., & Lipovetsky, V. A. 1996, ApJ, 463, 120
Thuan, T. X., Izotov, Y. I., & Lipovetsky, V. A. 1997, ApJ, 477, 661
Vanzi, L., Hunt, L. K., Thuan, T. X., & Izotov, Y. I. 2000, A&A, 363, 493
Witt, A. N., & Vijh, U. P. 2004, in ASP Conf. Ser. 390, Astrophysics of Dust, ed. A. N. Witt, G. C. Clayton, & B.T. Draine (San Francisco, CA: ASP), 115
Wolniewicz, L., Simbotin, I., & Dalgarno, A. 1998, ApJS, 115, 293
Zhang, Q., & Fall, S. M. 1999, ApJ, 527, L81
Zwart, S. F. P., Baumgardt, H., McMillan, S.L.W., Makino, J., Hut, P., & Ebisuzaki, T. 2006, ApJ, 641, 319